



## Report

Course Project: How Turbulence Decays and the Characteristics of  
Spatio-Temporal Deterministic Chaos.

Name: Paolo Giaretta  
Date: September 24, 2024  
Course: Turbulence ME-467  
Instructor: Tobias Schneider

# 1 Part I: Statistical Analysis of Turbulence

## 1.1 Data Analysis

The first part of this project focuses on the statistical analysis of turbulence from the experimental data obtained in the Warhaft Wind and Turbulence Tunnel at Cornell University [5]. The flow is propelled by a fan into a constant area wind tunnel. A grid is placed upstream of the measurement area to study the spatial evolution of grid-generated turbulence. Six hot-wire anemometers are evenly placed on the centerline at downstream distance  $d_1 = 1\text{ m}$  to  $d_6 = 1\text{ m}$  (Fig.1). The data was acquired at standard pressure and temperature, and stable thermal stratification. The measurements are obtained with a sampling frequency of  $f = 20\text{ kHz}$ , for a total of  $n = 10922567$  velocity measurements for each anemometer.

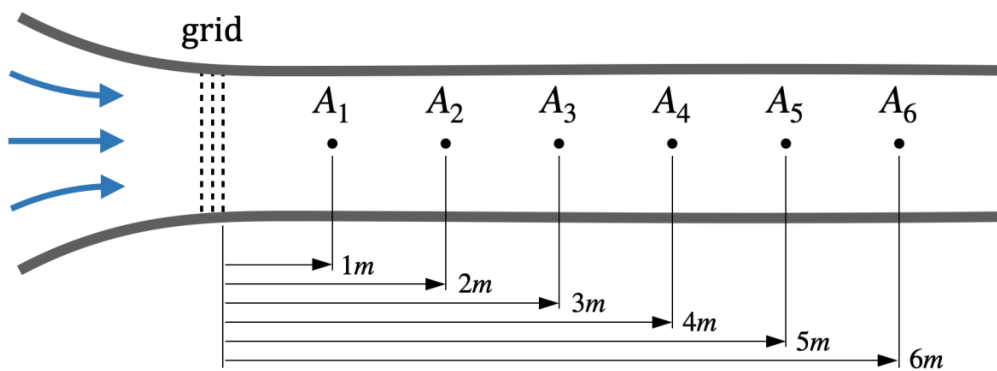


Figure 1: Schematic of the test section of the wind tunnel and position of hot-wire anemometers  $A_1$  to  $A_6$  with distances measured from the grid.

### 1.1.1 Velocity Signal in the Spatial Domain

The measured velocity field for each anemometer can be interpreted as spatial measurements under Taylor's frozen flow hypothesis. This hypothesis is valid under the condition that the mean velocity is significantly higher than the mean velocity fluctuations, i.e.,  $\sqrt{\langle u^2 \rangle} \ll U$ . When this condition is met, time measurements can be translated into spatial measurements using the mean velocity, according to the relation  $x = Ut$ . In the following sections, unless specified otherwise, all spatial measurements are based on the assumption that Taylor's frozen flow hypothesis holds true. The raw velocity measurements from each anemometer are shown in Fig.2 (covering the first  $\sim 2 \cdot 10^4$  samples) and in Fig.3 which provides a side-by-side comparison of all measurements.

From a qualitative inspection of plots, it appears that all anemometers measure virtually the same mean velocity. This observation is confirmed numerically by calculating the mean velocity  $U$ , which equals  $10.52\text{ m/s}$  for all six downstream positions. However, significant differences are observed in the intensity of velocity fluctuations. The variance in velocity measurements around the mean value consistently decreases with increasing distance of the probes from the grid.

At the first measuring station there are fluctuations in the order of  $\sim 2\text{ m/s}$ , whereas at the last measuring point fluctuations decrease to  $\sim 0.2\text{ m/s}$ . This trend is confirmed by the values of the turbulence intensity  $I = \sqrt{\langle u^2 \rangle}/U$ , as detailed in Table 1. The turbulence intensity decreases from 12.18% at the first measurement station to 1.75% at the last one. Given that the mean flow velocity remains nearly constant across downstream positions, the value of  $I$  is directly proportional to the average mean squared velocity fluctuations.

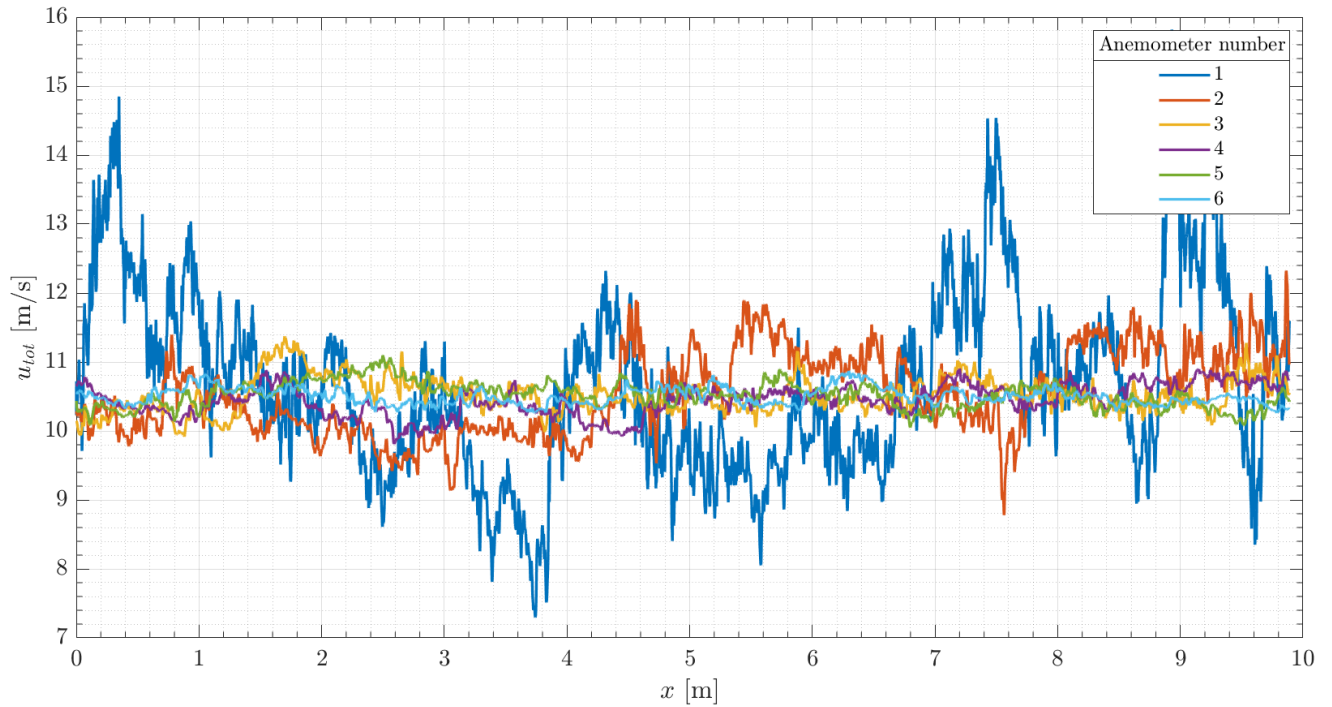


Figure 2: First  $\sim 2 \cdot 10^4$   $u_{tot}$  samples as a function of downstream distance (Plot A).

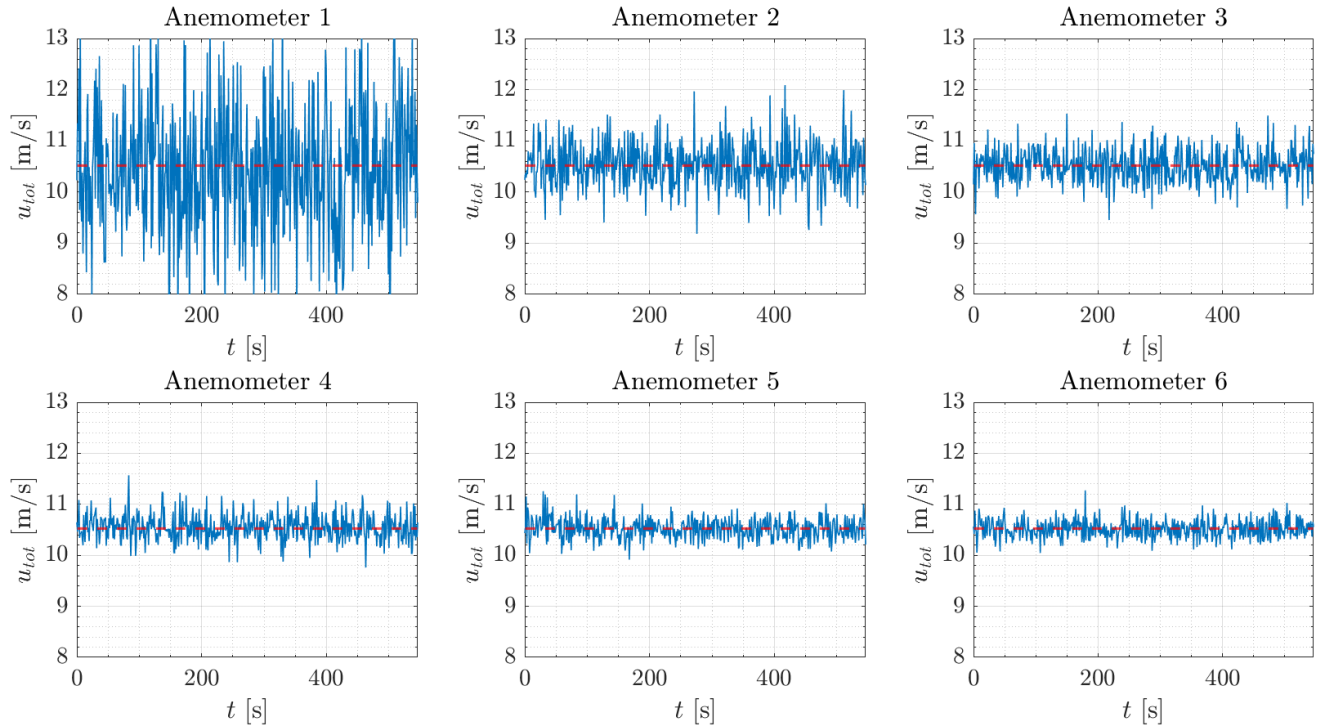


Figure 3: Side by side comparison of anemometers raw data.

The evolution of measurement statistics with downstream position is evident from the histograms in Fig.4. The bell-shaped probability density functions (PDFs) derived from the sampled data highlight the decreasing intensity of fluctuations downstream. Despite these changes in fluctuation intensity, both

Table 1: Table of results 1.

Param.	Dim.	$A_1$	$A_2$	$A_3$	$A_4$	$A_5$	$A_6$
$d$	$m$	1.0	2.0	3.0	4.0	5.0	6.0
$U$	$m/s$	10.52	10.52	10.52	10.52	10.52	10.52
$I$	%	12.18	4.70	3.20	2.50	2.05	1.75

the mean and median values remain constant.

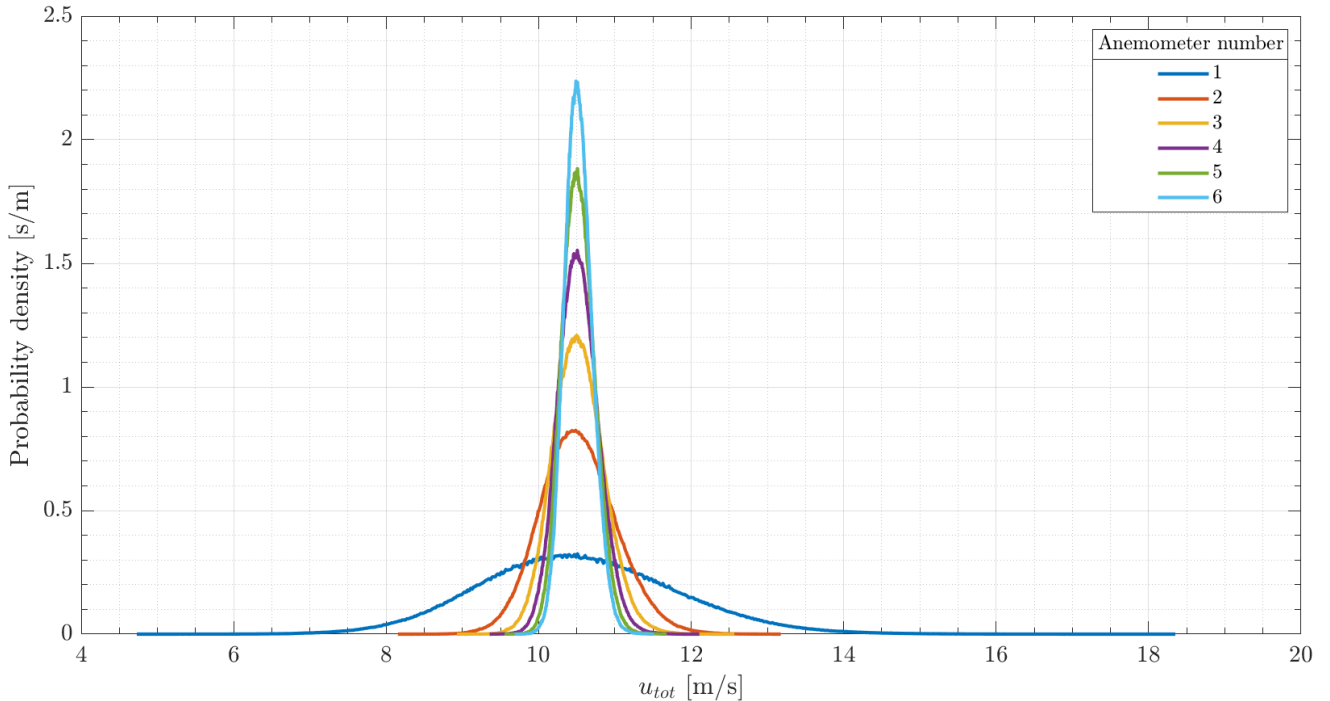


Figure 4: Histogram of  $u_{tot}$  measurements.

### 1.1.2 Considerations on the validity of Taylor Frozen flow hypothesis.

The whole data analysis relies on the possibility of interchanging temporal measurements of velocity differences into spatial ones (1). This is possible under Taylor's frozen flow assumption that turbulent structures do not change considerably during the time they are convected by the mean flow.

$$u(x, t + \tau) - u(x, t) \approx u(x - l, t) - u(x, t), \quad l = \tau U \quad (1)$$

The approximation introduced by this hypothesis arises from the error associated with assuming that the velocity fluctuations  $\hat{u}$  remain nearly constant during the timeframe  $\tau$  (2).

$$\hat{u}(x, t + \tau) \approx \hat{u}(x, t) \quad (2)$$

The first-order error introduced by this approximation in the Taylor expansion is:

$$\varepsilon = \tau \frac{\partial \hat{u}}{\partial t} \quad (3)$$

Two heuristic methods are presented to estimate the magnitude of error introduced by this approximation. The first one is likely to be more conservative and estimates a lower bound on the distance for which the flow can be considered frozen. The second one is an upper bound above which Taylor's assumption may no longer be applicable.

### Contribution at small scales.

According to Kolmogorov's theory, most of the kinetic energy contributions are due to the large scales, those comparable to the integral length. Bigger eddies produce larger variations in the velocity field, however their characteristic turnover time is significantly smaller. As a consequence, the time derivative of fluctuations  $\frac{\partial \hat{u}}{\partial t}$  is maximized by small-scale eddies. The effect of these fast fluctuations can be estimated numerically by computing the mean of the absolute velocity time derivative:

$$\left( \frac{\partial \hat{u}}{\partial t} \right)_{mean} = \frac{1}{N} \sum_{i=0}^{N-1} \left| \frac{\hat{u}_{i+1} - \hat{u}_i}{\Delta t} \right| \quad (4)$$

For the first anemometer, where the turbulence intensity is maximum, the mean time derivative is  $\sim 600 \text{ m/s}^2$ . The frozen flow hypothesis may become no longer valid when the first-order error becomes comparable with the mean velocity fluctuations, i.e.  $\tau \left( \frac{\partial \hat{u}}{\partial t} \right)_{mean} \approx \sqrt{\langle u^2 \rangle}$ . This corresponds to an advection distance  $\delta = \tau U = \langle u^2 \rangle U / \left( \frac{\partial \hat{u}}{\partial t} \right)_{mean} = 2.3 \text{ cm}$ . I would consider this as a lower bound on the applicability of Taylor's frozen flow approximation as this distance corresponds to the advection distance for the deformation of the smallest eddies (at least those that can be resolved within the sampling time window).

### Contribution at large scales.

The largest eddies in the flow are the structures that remain coherent for longer as they have the largest turnover times. When these structures are completely deformed it is reasonable to assume Taylor's frozen flow hypothesis is no longer applicable. To estimate the time derivative, I assume the characteristic velocity change in time due to the largest eddies is in the order of  $v_l = \sqrt{\langle \delta v_{||}^2(l) \rangle} \sim \sqrt{\langle u^2 \rangle}$  because most of the kinetic energy in the K41 theory belongs to the largest scales. The characteristic time scale for the deformation of eddies is the eddy turnover time  $t_l \sim l/v_l$  where  $l$  is in the order of the integral length scale  $l_0$ . Thus, we have the estimate  $\sqrt{\langle u^2 \rangle} \gg \tau \left( \frac{\partial \hat{u}}{\partial t} \right) \approx \tau \langle u^2 \rangle / l_0$ . This leads to a maximal advection distance  $\delta = \tau U \ll l_0/I = 3 \text{ m}$ . The same estimate can be obtained by simply comparing the integral-scale eddy turn-over time with  $\tau$ , i.e.  $\tau \ll t_l = l_0 / \sqrt{\langle u^2 \rangle} \Rightarrow \delta \ll l_0/I$ .

The cross-correlation between the first and second anemometers can serve as a check of whether the flow remains somewhat frozen for distances in the order of  $d = 1 \text{ m}$ , even though by looking at the turbulence intensity, we can infer the flow cannot be considered as fully frozen. If it remained perfectly correlated we would still expect a normalized cross-correlation (5) of around unity for a time shift  $\tau = d_{12}/U$  equal to the transit time of the flow between the first two anemometers.

$$\rho_{12} = \frac{\langle u_1(t)u_2(t + \tau) \rangle}{\sqrt{\langle u_1(t) \rangle \langle u_2(t) \rangle}} \quad (5)$$

Numerically the cross-correlation of the first two anemometers is in the order of  $\sim 7 \cdot 10^{-3}$ , proving the flow cannot be considered correlated at distances of  $1 \text{ m}$  or more.

#### 1.1.3 Correlation Length of the Velocity Signal

The autocorrelation of the measured velocity signals is computed as a function of correlation distance  $l$  as in (6), where  $u$  denotes the velocity fluctuations  $u = u_{tot} - U$ . For simplicity and (slightly) improved

performance the autocorrelation function has been computed in MATLAB with the function `autocorr`. It has been verified the results coincide with a straightforward manual implementation.

$$C(l) = \frac{\langle u(x+l)u(x) \rangle}{\langle u^2(x) \rangle} \quad (6)$$

By definition, the autocorrelation function (ACF) starts at unity. It successively sharply decreases with increasing  $l$ . For sufficiently large values of  $l$ , the signal loses coherence, and the autocorrelation functions oscillate around zero (Fig.5). The stronger fluctuating signals tend to lose coherence at smaller distances. A quantitative measure is provided by the correlation length  $L_c$ , defined as the downstream distance for which the ACF drops below  $1/e$ . The trend reported in Table 2 is consistent with the physical intuition of the flow. Near the inlet, the flow is more turbulent. As the flow moves downstream, energy is transferred to smaller scales where it is dissipated and the velocity fluctuations decrease in frequency and intensity. Therefore, it is expected the more rapidly changing flow will lose correlation with itself before.

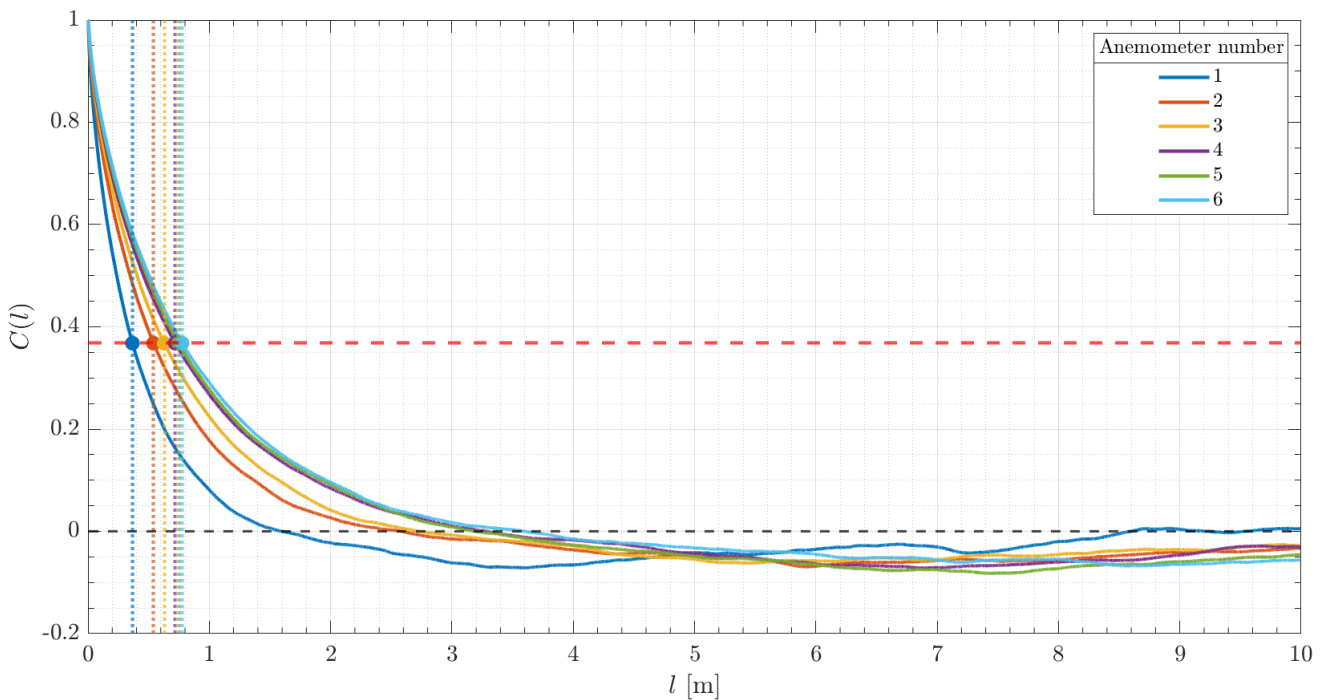


Figure 5: Autocorrelation functions of the six anemometers as a function of correlation length. Correlation lengths (as indicated by the dashed  $1/e$  threshold) increase for anemometers placed downstream. (Plot B)

It is possible to infer the integral scale length from (7). From a numerical perspective, it is necessary to define a suitable upper limit of integration to approximate the improper integral. It has been noticed that integration through quadrature, such as with the MATLAB built-in function `trapz`, is very sensitive to this upper limit. This is especially true for the first anemometer because the autocorrelation drops below zero and remains negative for a significant amount. Asymptotic fluctuations in autocorrelation also result in significant changes of  $L_{int}$  as the upper integration limit changes, even making  $L_{int}$  reach negative values. To choose a suitable upper limit we have to consider the autocorrelation becomes meaningless for correlation lengths  $l$  much larger than the characteristic length scale of the system, which is up to  $10^0 - 10^1$  m. First of all, it is reasonable to assume that once the fluid has already left the wind tunnel it should be uncorrelated with the turbulent flow that is just being generated. Second, the

underlying Taylor frozen flow hypothesis that allows taking velocity measurements from the time into the spatial domain loses validity for long times and correlation lengths. The numerical values of  $L_{int}$  are thus obtained by stopping the integration at the first zero-crossing of the autocorrelation function. This decision is supported by the idea that data after the autocorrelation has already dropped to zero, it is mostly influenced by noise. Therefore it may be reasonable to neglect the parts of the spectrum with a significant noise-to-signal ratio. In the literature, numerous alternative methods are proposed such as considering the minimum of the autocorrelation, second zero-crossing, or extrapolating the energy spectrum at very large ( $\rightarrow \infty$ ) scales [1].

$$L_{int} = \int_0^\infty C(l)dl \quad (7)$$

Table 2: Table of results 2.

Param.	Dim.	$A_1$	$A_2$	$A_3$	$A_4$	$A_5$	$A_6$
$L_C$	$m$	0.366	0.540	0.628	0.719	0.749	0.776
$L_{int}$	$m$	0.360	0.535	0.614	0.720	0.740	0.769

### 1.1.4 Energy Spectrum of the Flow

The spectral energy density, estimated for a finite downstream distance  $L$  is:

$$\tilde{E}(k) = \frac{1}{2} \left| \frac{1}{\sqrt{2\pi L}} \int_0^L u(x)e^{-ikx} dx \right|^2; \quad k \in \mathbb{R} \quad (8)$$

For positive wavenumbers, the energy spectrum is  $E(k) = \tilde{E}(k) + \tilde{E}(-k)$ . The Fast Fourier Transform (FFT) is used to calculate efficiently the energy spectrum for a wide range of wavenumbers. The following procedure is applied to ensure the correct normalization factors:

$$E(k) = \tilde{E}(k) + \tilde{E}(-k) = \left| \frac{1}{\sqrt{2\pi L}} \int_0^L u(x)e^{-ikx} dx \right|^2 = \frac{L}{2\pi} \left| \frac{1}{L} \int_0^L u(x)e^{-ikx} dx \right|^2 \approx \frac{L}{2\pi} \left| \frac{1}{N} \sum_{i=0}^N u_i e^{-ikx_i} \right|^2 \quad (9)$$

The first equality holds because inverting the sign of the wavenumber  $k$  in the Fourier integral results in complex conjugation, therefore the energy densities contained in  $k$  and  $-k$  are equivalent. The integral mean can be approximated by its discrete counterpart from the sampled signal  $u_i$ . By employing Taylor's frozen flow hypothesis the last spatial sum is converted into the temporal domain and it matches MATLAB `ifft` implementation. The discrete inverse Fourier Transform is calculated for the entire sampled signal, obtaining the energy spectrum at wavenumbers  $k_i = \frac{2\pi f}{U} \frac{i}{N}$ ,  $0 \leq i \leq N/2$ . The unfiltered energy spectrum (Fig.6) presents strong oscillations for high wavenumbers. Nevertheless, it is still possible to appreciate the presence of an inertial range following Kolmogorov K41 theory.

Parseval's theorem (10) relates the velocity field variance with the energy spectrum and can be used to check the proper normalization of the discrete Fourier transform. Parseval's relative error for the unfiltered energy spectrum of the first anemometer is  $9.13 \cdot 10^{-14}$ , which confirms the correct pre-factors.

It is necessary to filter the signal to understand the finer features of the energy spectrum. Many smoothening and de-noising approaches have been tested. Finding a satisfactory filtering operation has not been a trivial task. The energy spectrum, on a linear scale, presents a sharp decrease in amplitude

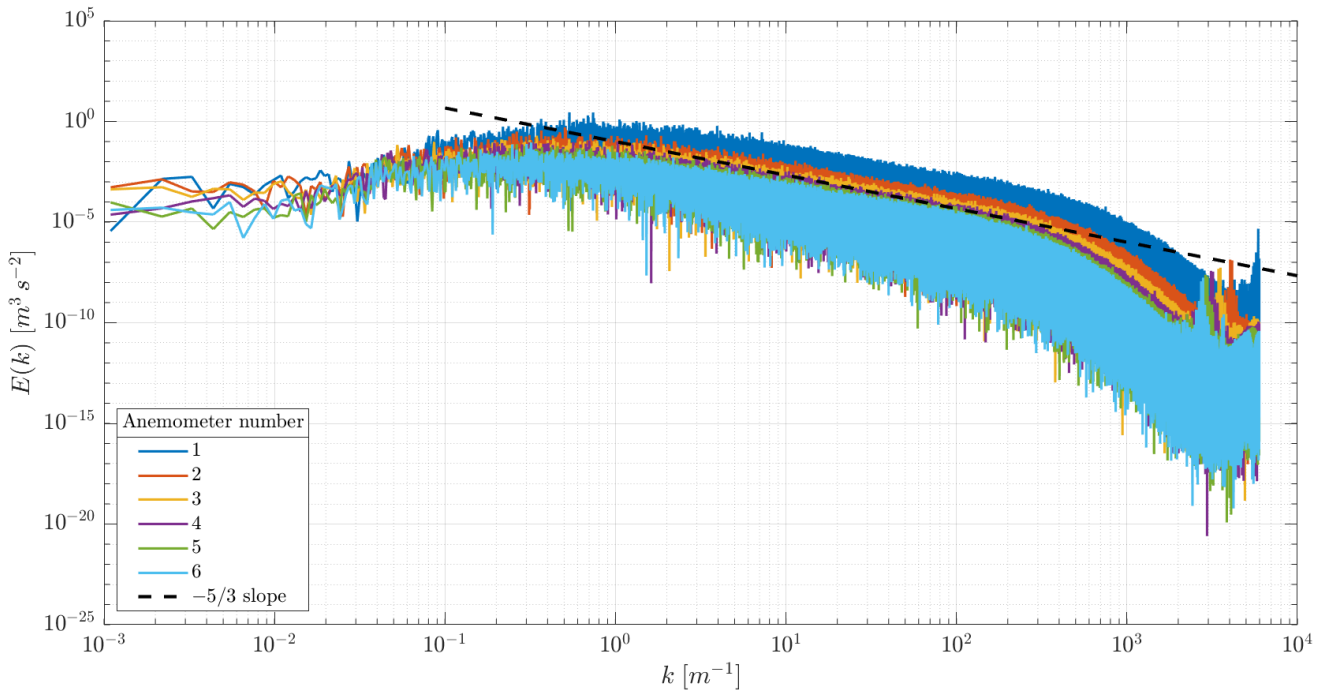


Figure 6: Unfiltered energy spectrum from Inverse Fast Fourier Transform.

for small wavenumbers. Thus, most lowpass filters tend to flatten excessively the energy spectrum at low wavenumbers when plotted in logarithmic axes. Furthermore, this distortion results in excessively high Parseval's errors up to 40%. The proposed solution is to resample the energy spectrum through linear interpolation with logarithmically equispaced wavenumbers. Successively the data is smoothed by a Gaussian moving mean procedure. This way, large wavenumber noise is filtered while minimizing distortion at low wavenumbers. This is confirmed by the much lower Parseval's error for the first anemometer of  $3 \cdot 10^{-4}$  after the filtering procedure.

$$\frac{1}{2} \langle u^2 \rangle = \int_0^\infty E(k) dk \quad (10)$$

The filtered energy spectrum is depicted in Fig.7. The filtered signal still presents significant noise in the  $10^{-3} - 10^{-1} m^{-1}$  wavenumber range. Even though numerous filtering techniques both in the linear and logarithmic domains have been tested, some more complex ad-hoc filtering techniques may produce more satisfying results. Moreover, the left-most part of the energy spectrum, which spans values of  $k \approx 10^{-3} - 10^{-2} m^{-1}$ , remains essentially flat. This part corresponds to length scales in the order of 15 – 100 m which are much larger than the characteristic dimensions of the wind tunnel and beyond the limits of applicability of the Taylor frozen flow hypothesis. Thus that part of the energy spectrum is assumed not to be physically meaningful in the characterization of turbulence for this experiment.

The K41 theory predicts the presence of an inertial range, spanning multiple orders of magnitude in energy density, with negligible dissipation and external forcing. In this region,  $E(k)$  follows a power law with exponent  $-5/3$ . For this prediction, we are making the following assumptions: **fully developed homogeneous and isotropic turbulence, stationarity of the velocity field, absence of forcing at small scales, finite dissipation limit at infinite Reynolds, and self-similar scaling of the structure functions** [2]. A discussion on the applicability of these hypotheses for the decaying turbulence under investigation is carried out in section 1.2.

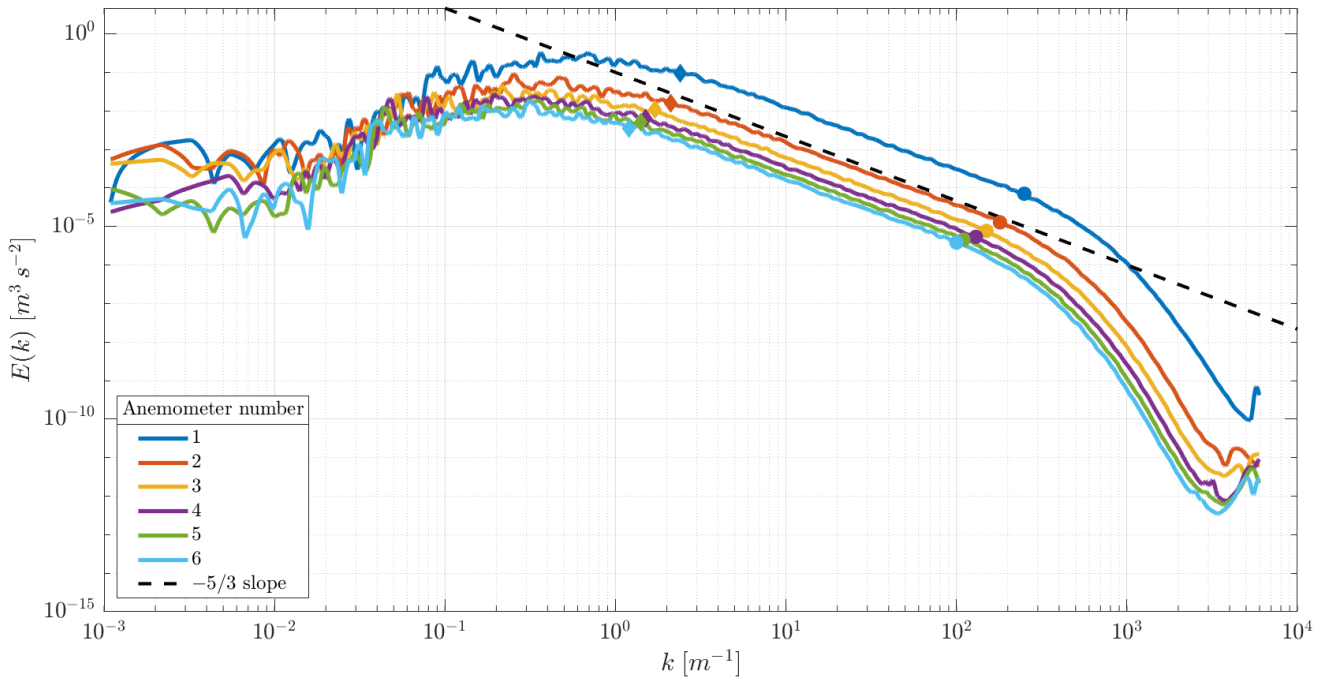


Figure 7: Filtered energy spectrum. The left and right extremes for the inertial range (respectively diamond and point markers) were used to estimate the integral and Kolmogorov scales. (Plot C)

At larger scales (comparable to the integral scale), energy is being injected into the cascade, whereas at smaller scales viscous dissipation starts to dissipate kinetic energy into heat. The experimental energy spectrum is consistent with Kolmogorov's theory. The inertial range is present and follows closely the predicted  $-5/3$  slope in logarithmic axes. The upper and lower limits of the inertial region are represented graphically with diamond and point markers respectively. Outside these limits, the energy spectrum starts to deviate from the predicted power-law trend. The upper limit may be used as an estimate of the integral length as it is the smallest scale at which energy is being injected into the cascade. To estimate the Kolmogorov scale  $\eta$ , it is possible to use the lower limit of the inertial range where the curve deviates from the  $-5/3$  predicted slope. The so-obtained wavenumbers  $K_d$  correspond to the scales at which viscosity starts to become relevant in the scale-by-scale energy budget. Usually, in experiments, this point corresponds to scales 30 times larger than Kolmogorov's. The values reported in the table are obtained by using 30 as the typical scaling factor, i.e.  $\eta \approx \frac{1}{30} \frac{2\pi}{k_D}$ .

The scale separation is in the order of  $\sim 2 \div 3 \cdot 10^3$ . This is consistent with the estimate based on the outer scale Reynolds number of  $\sim 1 \div 3 \cdot 10^4$  (see 1.1.5). The usual estimate predicts a separation between the Kolmogorov ( $\eta$ ) and integral scale ( $l_0$ ) of  $l_0/\eta \sim Re^{3/4} \approx 1 \div 2 \cdot 10^3$ , which is in good agreement with experimental data.

Table 3: Table of results 3.

Param.	Dim.	$A_1$	$A_2$	$A_3$	$A_4$	$A_5$	$A_6$
$L_{int,E}$	$m$	2.6	3	3.7	4.2	4.5	5.2
$\eta_E$	$mm$	0.8	1.2	1.4	1.6	1.9	2.1

### 1.1.5 The Dissipation Rate and Different Reynolds Numbers

The dissipation rate  $\epsilon$  can be estimated from the velocity fluctuations where energy is injected into the energy cascade (11).

$$\epsilon = \frac{1}{2} \frac{\sqrt{\langle u^2 \rangle^3}}{L_C} \quad (11)$$

From the dissipation rate, we can calculate the Taylor length scale  $\lambda$  (12) and Taylor Reynolds numbers  $Re_\lambda$  (13). The outer scale Reynolds number uses the integral length as the characteristic length scale (approximated by  $L_C$ ) and the root mean square velocity fluctuations as a velocity scale (14). The energy cascade transports energy from the large (integral) scales up to the small (viscous) scales. Therefore, the whole process is conditioned by the large-scale injection of energy, and it is reasonable to use a Reynolds number defined on the characteristic scales at the upper limit of the energy cascade. The reference value of the kinematic viscosity of air in standard conditions of  $\nu = 1.48 \cdot 10^{-5} m^2/s$  is used for all calculations.

$$\lambda = \sqrt{15\nu\langle u^2 \rangle/\epsilon} \quad (12)$$

$$Re_\lambda = \frac{\sqrt{\langle u^2 \rangle}\lambda}{\nu} \quad (13)$$

$$Re = \frac{\sqrt{\langle u^2 \rangle}L_C}{\nu} \quad (14)$$

Trends of  $\epsilon$ ,  $Re$ ,  $Re_\lambda$  (Fig.8, Fig.9) are consistent with the decrease of turbulence intensity with downstream distance. Given the mean flow velocity is approximately equal for all anemometers, the turbulence intensity is a measure of the total turbulence kinetic energy contained in the flow. As the flow moves downstream turbulence is transported progressively to smaller scales until it is dissipated by viscosity. Therefore the energy input at the top of the cascade becomes weaker over time. This results in a drastic decrease in the dissipation rate by more than two orders of magnitude. For the same reason, the weakening of turbulence at the largest scales is coherent with the trend in the outer scale Reynolds which represents non-dimensionally the turbulent behavior at the largest scales. The Taylor Reynolds number characterizes the behavior at an intermediate level in the energy cascade closer to the scales at which viscosity dominates. The Taylor length increases with downstream distance as the weaker turbulence is dissipated at relatively larger scales. The Taylor Reynolds number, however, follows the trend of I given the drastically lower turbulence kinetic energy.

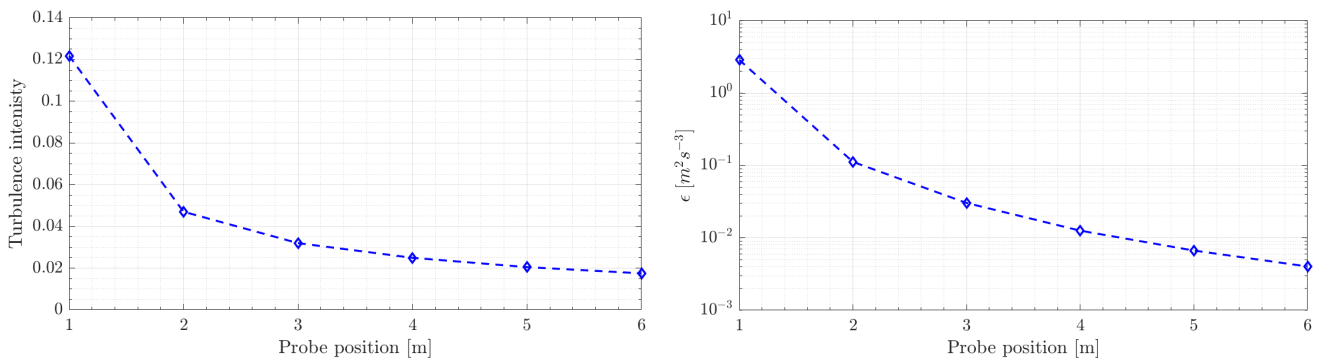


Figure 8: Taylor and outer Reynolds numbers.

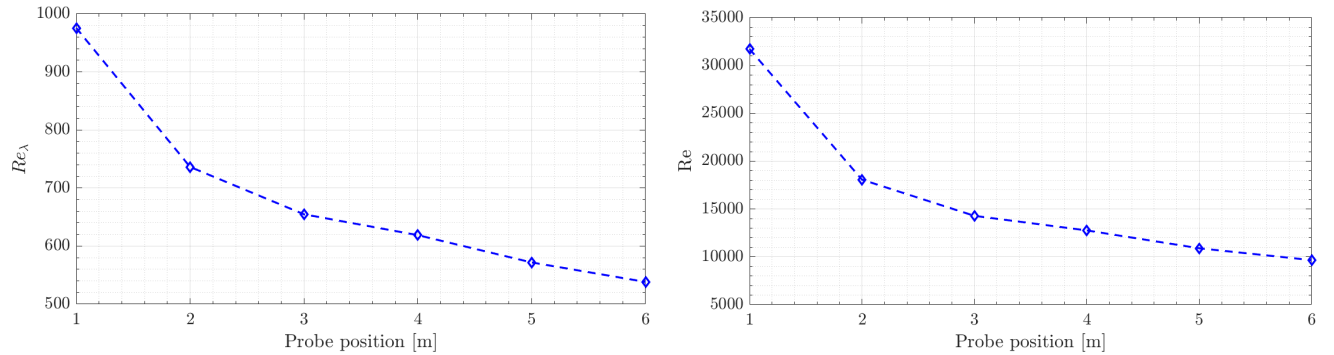


Figure 9: Turbulence intensity and dissipation rate.

Table 4: Table of results 4.

Param.	Dim.	$A_1$	$A_2$	$A_3$	$A_4$	$A_5$	$A_6$
$\epsilon$	$m^2/s^3$	2.874	0.1122	0.0303	0.0126	0.0067	0.0040
$Re_\lambda$	—	976	736	655	619	572	538
$Re$	—	$3.17 \cdot 10^4$	$1.81 \cdot 10^4$	$1.43 \cdot 10^4$	$1.28 \cdot 10^4$	$1.09 \cdot 10^4$	$0.97 \cdot 10^4$

### 1.1.6 Turbulence Decay

Under suitable assumptions (see 1.2), the spatial decay of turbulence may be approximated by a power-law. In this section, we assess the accuracy of this prediction for the grid-generated turbulence. Theoretically, most characteristic flow quantities follow a power law as a function of the downstream distance  $d$  (15-18), where  $d_0$  is the so-called virtual origin and  $h$  is the scaling exponent of the (infinitely) large scales.

$$l_0 \propto (d - d_0)^{1/(1-h)} \quad (15)$$

$$u_0 \propto (d - d_0)^{h/(1-h)} \quad (16)$$

$$Re \propto (d - d_0)^{(1+h)/(1-h)} \quad (17)$$

$$\mathcal{E} \propto (d - d_0)^{2h/(1-h)} \quad (18)$$

$l_0$  and  $u_0$  represent respectively the integral scale and velocity,  $Re$  the outer scale Reynolds and  $\mathcal{E}$  the turbulence kinetic energy. The overall kinetic energy per unit mass of the flow is defined as  $\mathcal{E} = \langle u^2 \rangle + \langle v^2 \rangle + \langle w^2 \rangle$ . Under the assumption of *isotropy* of the turbulent flow the statistics along the three spatial directions  $x, y, z$  are equal, thus  $\langle u^2 \rangle = \langle v^2 \rangle = \langle w^2 \rangle$ . This implies  $\mathcal{E} = \frac{3}{2} \langle u^2 \rangle$ . It is important to note that the hypothesis of isotropy at the anemometers' downstream positions is not trivial. It shall be experimentally verified for this setup, given the clear directionality induced by the grid-flow interaction in turbulence generation. To experimentally extrapolate the best fitting parameters the following three methods are proposed and compared.

Table 5: Table of results 5.

Param.	Dim.	$A_1$	$A_2$	$A_3$	$A_4$	$A_5$	$A_6$
$\mathcal{E}$	$m^2/s^2$	2.46	0.367	0.170	0.103	0.070	0.051

#### Automatic fitting.

The first possibility is to find the 'best' fitting parameters  $d_0$  and  $h$  by employing a suitable non-linear fitting numerical scheme. The function to be fitted (19) depends on three parameters: the proportionality constant  $C$ , the virtual origin  $d_0$ , and the scaling exponent  $q$ , where  $h = q/(q+2)$ .

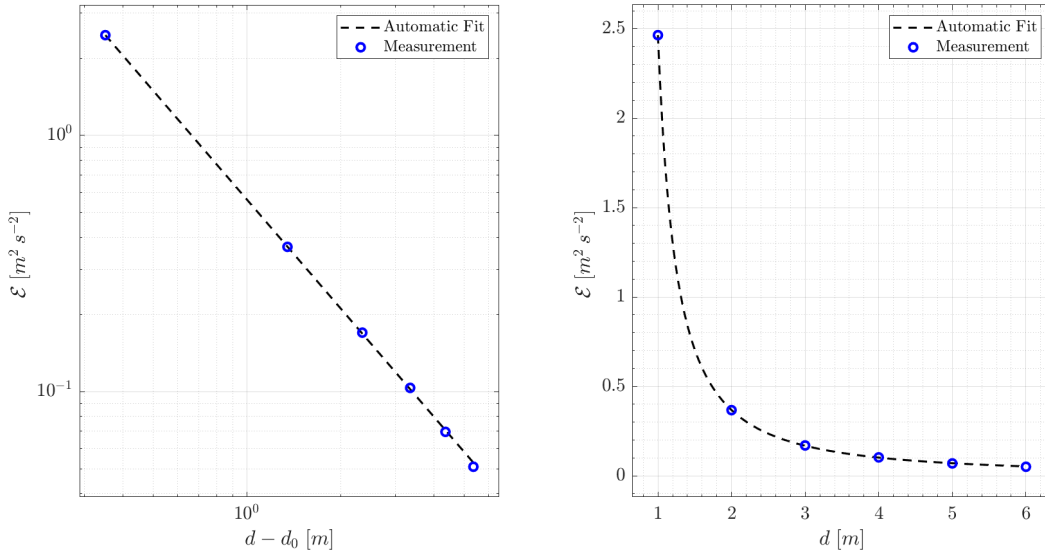


Figure 10: Automatic fitting of kinetic energy.

$$\mathcal{E} = C(d - d_0)^{2h/(1-h)} = C(d - d_0)^q. \quad (19)$$

The fit has been obtained by MATLAB non-linear fitting routine `fitnlm` based on the iteratively reweighted least squares algorithm. The power law (19) corresponds to a straight line in a plot of  $\mathcal{E}$  against  $d - d_0$  in logarithmic axes. The fit appears to be very precise (10) and leads to values  $d_0 = 0.6492\text{ m}$  and  $h = -2.392$ .

### Graphical fitting.

A second option is to assess graphically the best fitting parameters. As before, if the points were to follow exactly the theoretical scaling relation, they would lie on a straight line in the log-log plot of  $\mathcal{E}$  against  $d - d_0$ . It has been chosen to select eight equispaced guess values of  $d_0$  in the interval  $[0.5, 0.8]$ . For each of them, the measured data points are plotted in logarithmic axes and compared to the best corresponding least squares fit (11).

For the extreme values of  $d_0$ , it is clear the datapoints present some concavity and fail to follow accurately a straight line. By visual inspection, it appears the best two fits are for values  $d_0 = 0.63\text{ m}$  and  $d_0 = 0.67\text{ m}$ , however, it is not trivial to decide which of the two is the better approximation. This observation might be used as an acceptable range of values of the virtual origin that can be extrapolated from the measured data. For the range  $d_0 = 0.63 \div 0.67\text{ m}$  the range of the scaling exponent  $h$  from the linear regression coefficients is  $h = -2.61 \div -2.26$ .

### Integral scale fitting.

The last method comes from the scaling relation of the kinetic energy as a function of the integral length  $l_0$  (20).

$$\mathcal{E} \propto l_0^{2h} \quad (20)$$

The scaling exponent can be determined graphically by plotting  $\mathcal{E}$  against  $l_0$  in logarithmic axes. The theoretical prediction through least squares fit gives an estimate of  $h = -2.499$ . The graphical fitting is compared with theoretical predictions for Saffman's decay ( $2h = -3$ ), Loitsyanski's decay ( $2h = -5$ ),

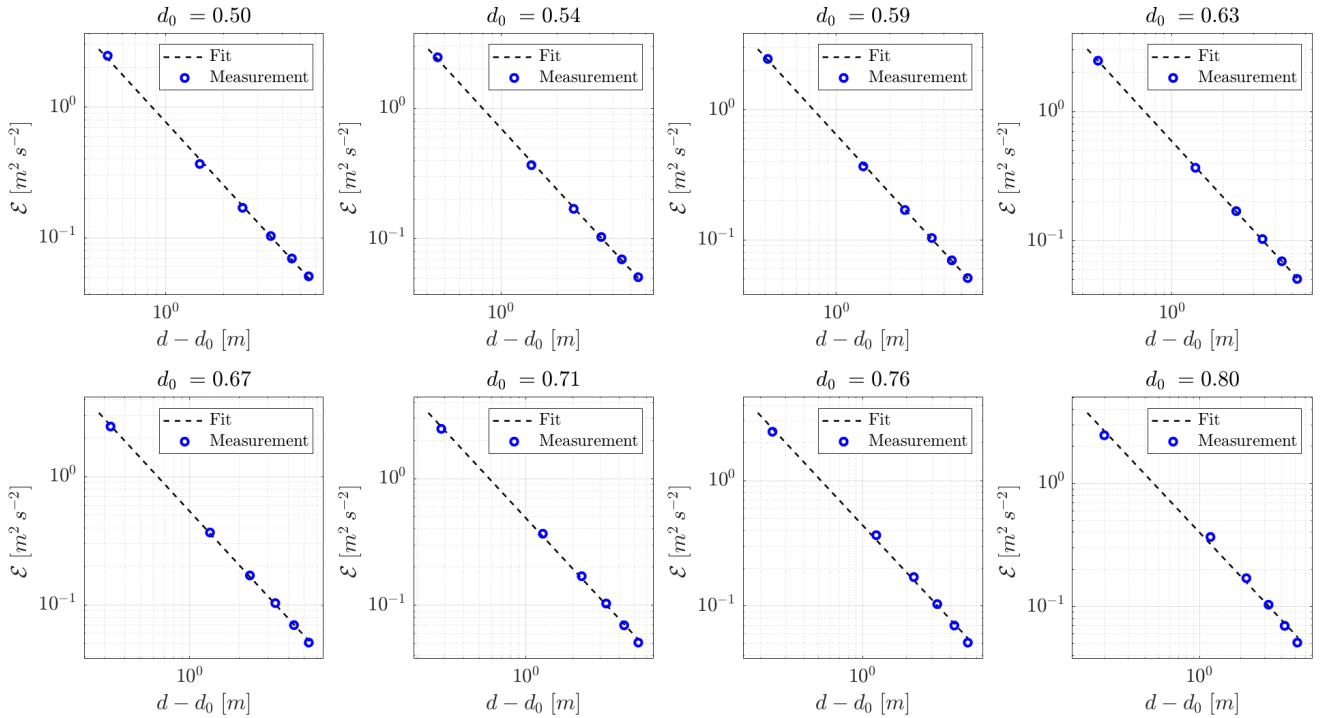


Figure 11: Graphical fitting procedure. The points are fitted in logarithmic axes for a range of virtual origins  $d_0 \in [0.5, 0.8]$ . (Plot D)

and self-similar decay ( $2h = -2$ ) (Fig.12). The best matching prediction is Loitsyanskii's decay, which corresponds to  $h = -2.5$ . The fitting, however, is not perfect as anemometers 4 and 6 deviate from both the least squares fit and best theoretical prediction. Once the value of the scaling exponent has been set to Loitsyanskii's prediction the virtual origin can be found by fitting  $\epsilon = C(d - d_0)^{2h/(1-h)}$ , inverting the relation as  $\epsilon^{(1-h)/(2h)} = Ad + B$ , where  $A = C^{(1-h)/(2h)}$ , and  $B = -d_0C^{(1-h)/(2h)}$ . This results in an estimate of  $d_0 = 0.6674\text{ m}$  (Fig.13).

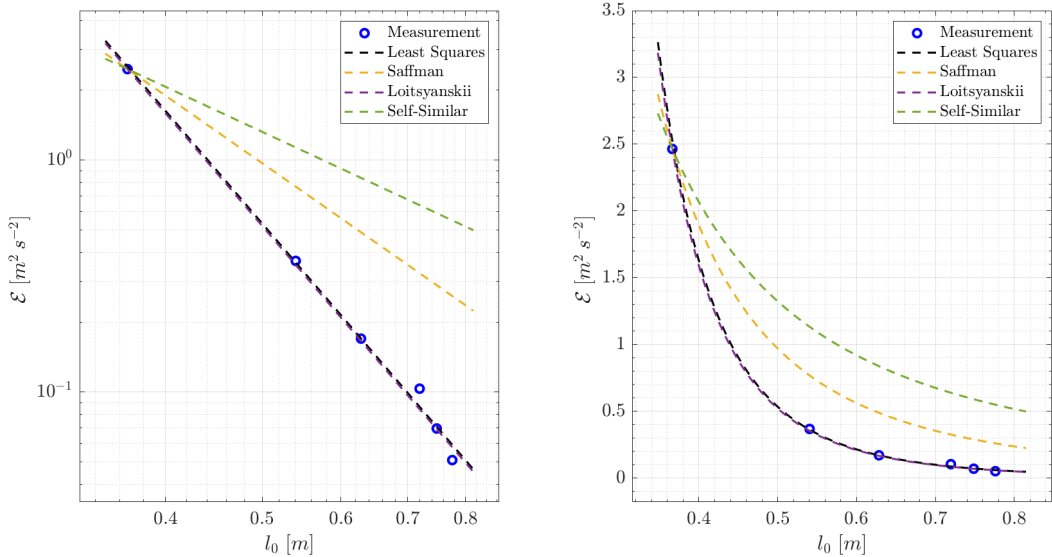


Figure 12: Integral scale fitting and theoretical predictions. (Plot E)

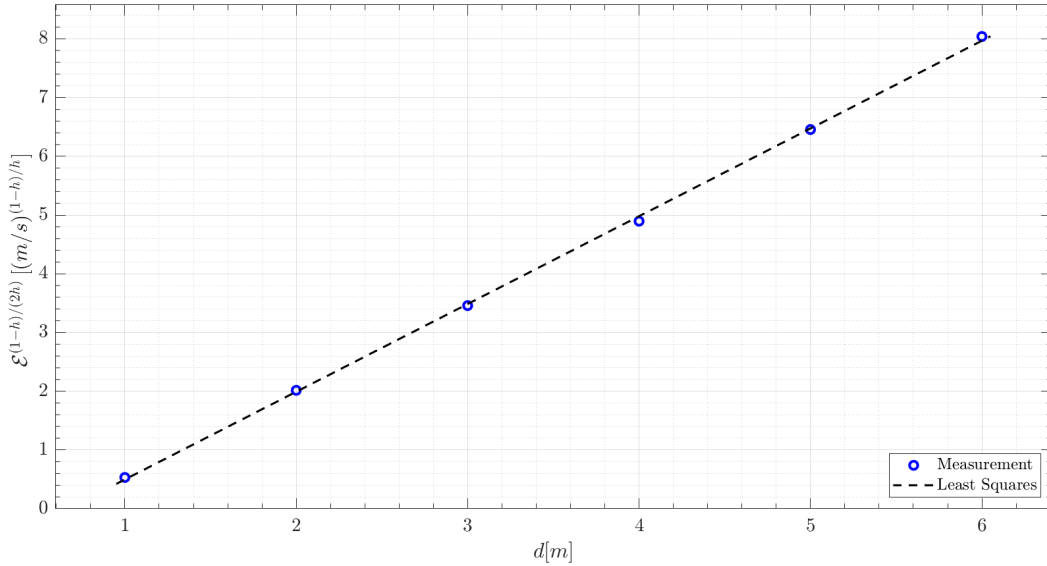


Figure 13: Fit of  $d_0$  for  $h = -5/2$  (Loitsyanskii).

The three approaches lead to similar estimates of the virtual origin and scaling exponent (Table 6). Each method presents peculiar advantages and disadvantages:

- For the **automatic fitting**, the non-linear fit can approximate the experimental trend very precisely without much external input. However, there is very little control over the final error estimate and final converged solution found by the algorithm. Particularly, there is always a risk the non-linear procedure starts to overfit noise, leading to poorer generalization of the fitted model.
- The **graphical fitting** procedure is more qualitative in the assessment of which  $d_0$  leads to the datapoints following more closely a linear trend. This lack of precision, however, may be turned into a confidence estimate of the accuracy of the proposed fit. Unlike the previous technique, there is some control on the fitting uncertainty.
- The **integral scale fitting** approach is backed by theoretical predictions. In this way, any reasonable fit can be compared to the expected predictions assessing how much measured data deviates from it. From the comparison, it may be possible to assess the errors committed in the measurement procedure or due to the underlying hypothesis of the theoretical decay.

Table 6: Fitted values of scaling exponent and virtual origin.

Fit	$h$	$d_0$
Automatic	-2.392	0.6492 m
Graphical	-2.61 ÷ -2.26	0.63 ÷ 0.67 m
Integral Scale (Loitsyanskii)	-2.5	0.6674 m

The energy spectrum  $E(k)$  is predicted to scale as  $E(k) \sim k^{-(1+2h)}$  for length scales sufficiently larger than the integral length scale. The scaling prediction obtained with the previous techniques (using Loitsyanskii as a reference) matches the energy spectrum reasonably well but not perfectly (Fig.14). Unlike the K41 inertial range scaling, the range of wavenumber for which the prediction is accurate does not span multiple decades. The trend is followed accurately only for a fraction of wavenumbers in the  $10^{-2} - 10^{-1}$  range. Moreover, the relatively noisy data makes it challenging to fully appreciate

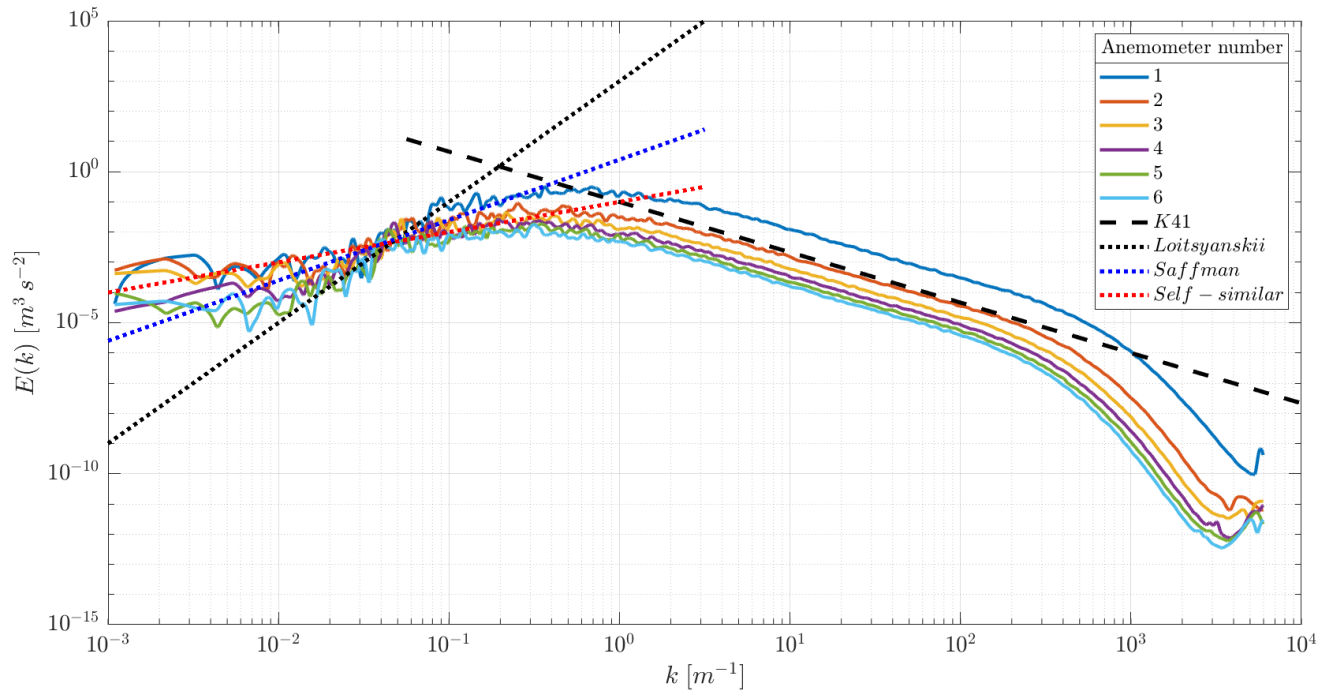


Figure 14: Energy spectrum with turbulence decay prediction. (Plot F)

deviations from the fitted trend. It is still possible to observe more deviations in the predicted slope for the first anemometer compared to the last one. This may suggest the theoretical prediction is more accurate if the turbulence intensity (and kinetic energy) are lower.

The virtual origin  $d_0$  for all fitting procedures lies in the  $0.6 - 0.7 m$  range. It is located between the grid and the first anemometer. It is reasonable to assume it is not just a simple fitting parameter but it marks a location where the flow properties change drastically. Indeed,  $d_0$  is obtained by extrapolating the power law decay upstream of the anemometers. I assume the virtual origin correlates with the position of the point upstream of the anemometers at which the turbulence decay starts to follow a power law. This is aligned with the physical intuition of the flow. Even though turbulence arises from the flow-grid interaction, there is some finite downstream distance before most of the turbulent motion is generated and starts decaying with the behavior reported in Fig.14, which requires a restoration of all allowable Navier-Stokes symmetries in a statistical sense and the establishment of the K41 energy cascade. For these reasons, I would not expect the virtual origin to change drastically if fitting the power law for another quantity, such as integral scale or Reynolds.

## 1.2 Interpretation and Discussion

The law of turbulence decay for unforced turbulence is based upon the *principle of permanence of large eddies*, which states:

**Principle of permanence of large eddies** *If the flow is freely decaying (no external force) and initially possesses the property of asymptotic self-similarity with scaling exponent  $-\frac{5}{2} < h < 0$  and a constant  $C$ , then this property is preserved for all later times with the same  $h$  and  $C$  [2].*

Where the hypothesis of *infrared self-similarity* refers to the large-scale ( $l \rightarrow \infty$ ) scaling similarity:

$$v_l = \sqrt{\langle u_{\parallel}^2(l) \rangle} \sim Cl^h \quad (21)$$

Note that we are assuming the large-scale restoration of dynamical symmetries of homogeneity and isotropy to justify the expression of  $v_l$  as a function of  $l$  only. Under the assumption the decay remains turbulent, i.e. the outer Reynolds number  $Re \gg 1$ , we can assume there exists a time-dependent integral scale length  $l_0$ , below which the behavior is compatible with the usual K41 energy cascade. The scaling (21) can be rephrased in terms of the integral scale properties:

$$v_0 \sim Cl_0^h \quad (22)$$

The validity of K41 in the decaying case provides a scaling prediction of the dissipation rate  $\varepsilon \sim v_l^3/l$  for lengths in the inertial range. According to Kolmogorov, the energy dissipation remains constant in the inertial range. Thus, calculating the scaling for the upper limit of the inertial range, we can evaluate the rate of dissipation of mean energy:

$$\frac{dE}{dt} \sim \frac{dv_0^2}{dt} \sim -\varepsilon \sim -\frac{v_0^3}{l_0} \quad (23)$$

From the hypothesis of large-scale self-similarity, we obtain an ODE that leads to a power-law for the integral scale time-evolution (24), as well as for the quantities in (15-18).

$$\frac{d}{dt} (l_0^{2h}) \sim -C l_0^{3h-1} \quad (24)$$

To derive Kolmogorov's theory, it is assumed the flow is stationary (in a statistical sense). By definition, this is in direct contradiction with the non-stationary process of turbulence decay. If all other K41 assumptions remain valid, K41 predictions may hold even in non-stationary conditions and without external forcing. The limit factor of the decay process is the transfer of energy from the very large (asymptotic) scales to the upper limit of the inertial range. The predicted energy cascade presents faster dynamics, therefore it sees a quasi-stationary large-scale flow. This assumption allows us to assume the validity of Kolmogorov's theory conditioned on a time-dependent integral scale  $l_0$ .

The K41 predictions remain valid as long as the flow remains turbulent, i.e.  $Re \gg 1$ . If the scaling exponent  $h < -1$ , then the power-law scaling predicts  $Re \rightarrow 0$  as  $t \rightarrow \infty$ . When Reynolds becomes sufficiently low, the flow transitions from turbulent decay to pure viscous dissipation. Given that viscous forces are proportional to velocity magnitude, the decay becomes exponential. The *permanence* of turbulence refers to the empirically slow decay of turbulence due to the power law trend, instead of exponential. Even though it is not the case for this experiment, in the case of  $h > -1$ , the power-law scaling predicts  $Re \rightarrow \infty$  as  $t \rightarrow \infty$ . This is a consequence of how the outer-scale Reynolds number is defined. For  $h > -1$  the increase in integral length scale is faster than the dissipation of mean kinetic energy  $\langle u^2 \rangle$ . This limit, however, is only theoretical. As the energy content of the flow decreases, the regime will transition to viscous dissipation and, eventually, the Reynolds number will vanish.

## 2 Part II: Quantitative characterization of chaos

### 2.1 Properties of the governing equation

The Kuramoto-Sivashinsky-Equation (KSE) (25) under the assumptions of L-periodic boundary conditions preserves the mean value of the field  $u(x, t)$ .

$$\begin{aligned} \frac{\partial u}{\partial t} &= -u \frac{\partial u}{\partial x} - \frac{\partial^2 u}{\partial x^2} - \nu \frac{\partial^4 u}{\partial x^4} \\ x \in [-L/2, L/2] \quad u(-L/2, t) &= u(L/2, t) \quad \forall t \in \mathbb{R}^+ \end{aligned} \quad (25)$$

To prove the mean preserving properties of the dynamical system, two key observations are first presented and proved.

1. The derivative of a differentiable L-periodic function is L-periodic.
2. The spatial mean of the derivative of a L-periodic function over the entire spatial domain vanishes.

*Proof:*

1. Let  $f : \mathbb{R} \rightarrow \mathbb{R}$  be differentiable and L-periodic, i.e  $f(x + L) = f(x) \forall x \in \mathbb{R}$ . Then by differentiating both sides of the equation we have  $f'(x + L) = f'(x)$ , implying  $f'$  is L-periodic. By repeating this argument the same applies for higher-order derivatives, provided they exist.
2. The spatial mean operator applied to the derivative of a function  $f$  satisfies  $\langle f' \rangle = \frac{1}{L} \int_{-L/2}^{L/2} f' dx = f(L/2) - f(-L/2)$ . By requiring L-periodicity of  $f$  the last term vanishes, as well as the spatial mean of  $f'$ .

Applying the spatial mean operator on both sides of (25), the RHS vanishes by observations 1-2:

$$\langle \frac{\partial u}{\partial t} \rangle = \langle -u \frac{\partial u}{\partial x} \rangle - \langle \frac{\partial^2 u}{\partial x^2} \rangle - \langle \nu \frac{\partial^4 u}{\partial x^4} \rangle = -\langle \frac{\partial (u^2/2)}{\partial x} \rangle - \langle \frac{\partial^2 u}{\partial x^2} \rangle - \nu \langle \frac{\partial^4 u}{\partial x^4} \rangle = 0 \quad (26)$$

$$0 = \langle \frac{\partial u}{\partial t} \rangle = \frac{1}{L} \int_{-L/2}^{L/2} \frac{\partial u}{\partial t} dx = \frac{d}{dt} \left( \frac{1}{L} \int_{-L/2}^{L/2} u dx \right) = \frac{d}{dt} \langle u \rangle \quad (27)$$

The exchange of the time derivative operator and spatial mean is justified by the sufficient regularity of  $u$  (at least differentiable) over the bounded interval  $[-L/2, L/2]$ . Thus, the spatial mean is preserved under the KSE dynamics. Another property of the KSE is the equivariance under reflection about the origin,  $u(x, t) \mapsto -u(-x, t)$ . By defining  $\hat{x} = -x$ , the spatial derivative operators become:

$$\begin{aligned} \frac{\partial}{\partial \hat{x}} &= \frac{\partial}{\partial x} \frac{\partial x}{\partial \hat{x}} + \frac{\partial}{\partial t} \frac{\partial t}{\partial \hat{x}} = -\frac{\partial}{\partial x} \\ \frac{\partial^2}{\partial \hat{x}^2} &= -\frac{\partial}{\partial \hat{x}} \left( \frac{\partial}{\partial x} \right) = \frac{\partial^2}{\partial x^2} \\ \frac{\partial^4}{\partial \hat{x}^4} &= \frac{\partial^2}{\partial \hat{x}^2} \left( \frac{\partial^2}{\partial x^2} \right) = \frac{\partial^4}{\partial x^4} \end{aligned} \quad (28)$$

Substituting in (25) the differential operators with those obtained by the transformation  $u(x, t) \mapsto$

$-u(-x, t) = \hat{u}(\hat{x}, t)$  we obtain the following terms:

$$\begin{aligned}\frac{\partial u}{\partial t} &= -\frac{\partial \hat{u}}{\partial t} \\ u \frac{\partial u}{\partial x} &= (-\hat{u}) \left( -\frac{\partial (-\hat{u})}{\partial \hat{x}} \right) = -\hat{u} \frac{\partial \hat{u}}{\partial \hat{x}} \\ \frac{\partial^2 u}{\partial x^2} &= \frac{\partial^2 \hat{u}}{\partial \hat{x}^2} \\ \frac{\partial^4 u}{\partial x^4} &= \frac{\partial^4 \hat{u}}{\partial \hat{x}^4}\end{aligned}\tag{29}$$

Therefore, the transformed variables satisfy the KSE equation (30), and the reflection about the origin is an equivariance.

$$\frac{\partial \hat{u}}{\partial t} = -\hat{u} \frac{\partial \hat{u}}{\partial \hat{x}} - \frac{\partial^2 \hat{u}}{\partial \hat{x}^2} - \nu \frac{\partial^4 \hat{u}}{\partial \hat{x}^4}\tag{30}$$

## 2.2 Chaotic behavior of the Kuramoto–Sivashinsky equation

### 2.2.1 Qualitative investigation

The three dynamics outlined in the following table are investigated to have a qualitative understanding of the complexity of the dynamics of the KSE, and its dependence on the domain length  $L$  and symmetry constraint. The integration has been carried out for a duration of  $t_{max} = 750$  time units, time step  $dt = 0.1$ , and spatial discretization in  $N = 64$  nodes. The integration scheme is the ETDRK4 time-stepping approach in Fourier space [4].

Table 7: Numerical simulation conditions

system	domain length	initial condition	reflection symmetry
1	$L = 22.0$	$u(x, 0) = \sin\left(\frac{2\pi x}{L}\right) + \frac{3}{2}\cos\left(\frac{4\pi x}{L}\right)$	No
2	$L = 38.6$	$u(x, 0) = \sin\left(\frac{2\pi x}{L}\right) + \frac{3}{2}\cos\left(\frac{4\pi x}{L}\right)$	No
3	$L = 38.6$	$u(x, 0) = \sin\left(\frac{2\pi x}{L}\right)$	Yes

The space-time contours of  $u(x, t)$  for each evolution (Fig.15) highlight differences in the complexity of the dynamics between the three systems. Comparing system 1 with system 2, it appears that increasing the domain length leads to far richer and more complex dynamics. The second system presents a wider range of spatiotemporal frequencies in the plotted chaotic structures. In particular, smaller wavelengths and frequencies can be observed, with very rapid changes among neighboring values. This observation indicates the effect of confinement is stabilizing. Reducing the periodic domain length leads to progressively less chaotic behavior, until for values of  $L \sim 17$  the solution converges towards a steady state (Fig.16). Comparing the evolutions of systems 2 and 3, the symmetry constraint reduces dynamical complexity within the symmetric subspace. In particular, the last system exhibits some well-defined oscillation frequencies in time with quasi-periodic behavior. In the second system, the structures appear to be much less coherent in space and time. For similar reasons, it appears that the first dynamics is more complex than the last one, albeit the difference is not as evident as for the second evolution. From a

qualitative viewpoint, I would rank the complexity of the three simulations in ascending order as follows:

$$\boxed{\text{System 3} < \text{System 1} < \text{System 2}}$$

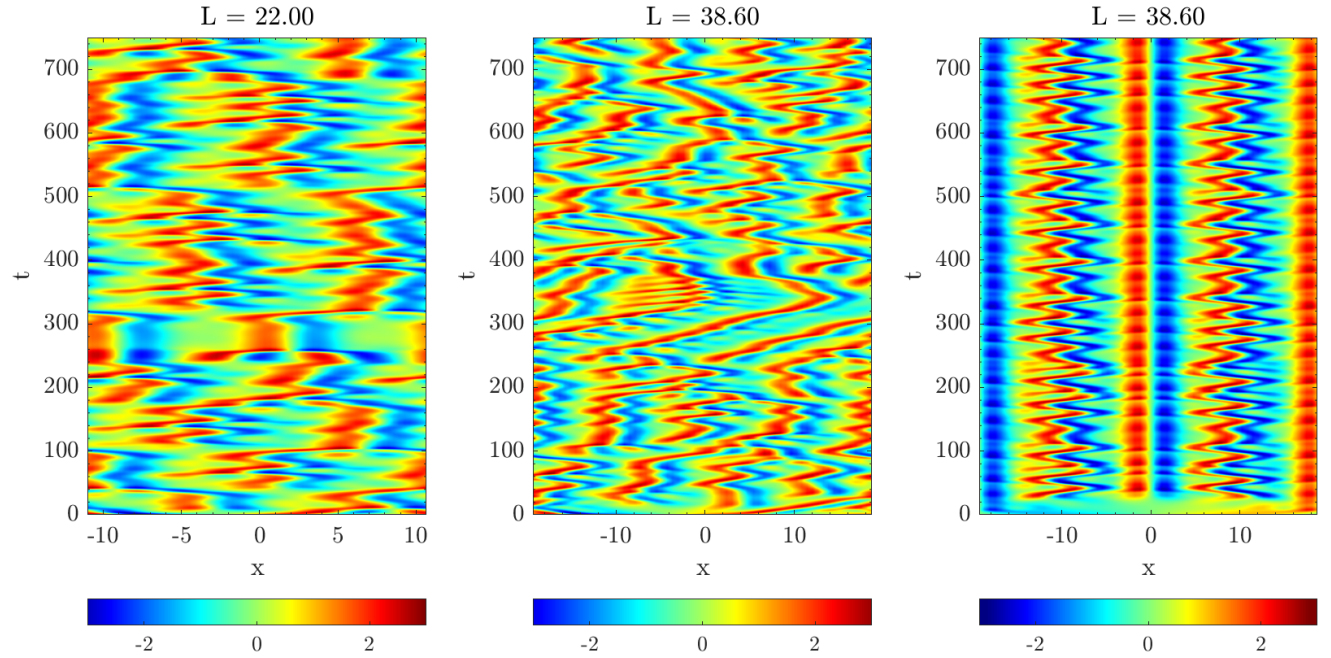


Figure 15: Space-time contours. (Plot A)

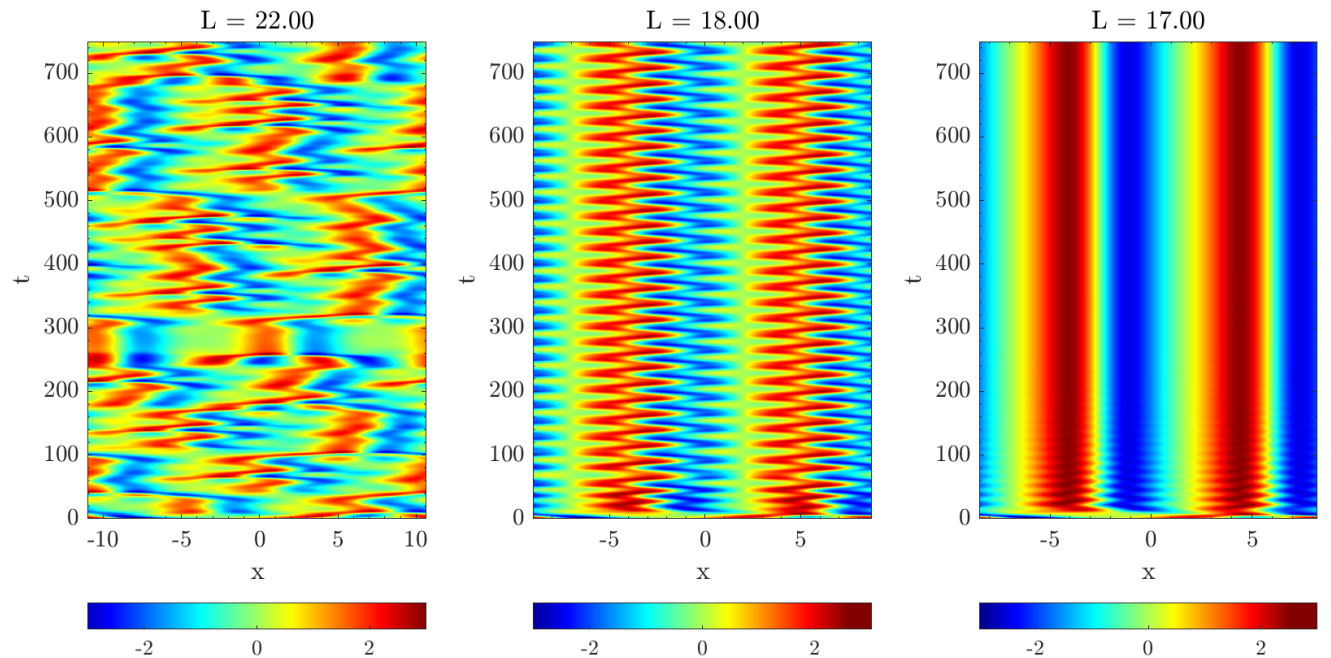


Figure 16: Effect of confinement on system 1.

### 2.2.2 Quantitative characterization

The qualitative observations can be formalized by a quantitative analysis of the chaotical properties of the dynamical system. The leading Lyapunov exponent provides information regarding the predictability of the system. In particular, Lyapunov exponents describe the exponential growth rate of perturbations due to the chaotic nature of the dynamical system. The largest positive exponent determines the most unpredictable dynamics arising from the KSE. For the three systems, the 10 largest Lyapunov exponents have been calculated numerically through the so-called *standard algorithm* based on repeated renormalizations through QR factorization of the time evolution of perturbations. The final estimates, summarized in the following table, are computed for a  $t_{max} = 10^4$  time units and for  $M = 5 \cdot 10^3$  renormalization steps.

Table 8: Table of results

	$L = 22.0$ full state space	$L = 38.6$ full state space	$L = 38.6$ symmetric subspace
$\chi_1$	0.0447	0.0741	0.0546
$\chi_2$	0.0022	0.0470	7.238e-5
$\chi_3$	2.95e-4	0.0253	-0.1813
$\chi_4$	-0.0048	4.21e-4	-0.2860
$\chi_5$	-0.1871	-1.95e-4	-0.3309
$\chi_6$	-0.2558	-0.0073	-0.3884
$\chi_7$	-0.2938	-0.0560	-0.5877
$\chi_8$	-0.3083	-0.1165	-0.7260
$\chi_9$	-1.9637	-0.1914	-2.277
$\chi_{10}$	-1.9682	-0.2607	-4.253
$D_{KY}$	4.23	7.71	2.30

The iterative numerical estimates of the leading Lyapunov exponents number are depicted in (Fig.17). As can be seen, for all systems the Lyapunov exponents guesses stabilize after  $10^4$  iterations. The second system's convergence is slightly slower, with pronounced fluctuations in the estimates at  $\sim 10^2$  iterations. This is likely to be a consequence of the richer and more chaotic dynamics of the second system. By inspection of (Fig.18), the iterative updates of the exponents decrease steadily with increasing iteration number. Even though significant fluctuations are present, the maximal update step size decreases following an almost first-order rate (red dashed line). When the algorithm terminates, all the update step sizes  $|\chi_{i+1} - \chi_i|$  are upper bounded by  $2 \cdot 10^{-4}$ .

In all cases, it is expected that at least one Lyapunov exponent vanishes [3]. This is due to the fact perturbations locally aligned with the flow direction do not experience exponential growth. For the first two systems, continuous spatial translation constitutes an equivariance. This additional symmetry implies the existence of one additional zero Lyapunov exponent. Indeed, as the system evolves in phase space, a perturbation that has the net effect of a spatial translation does not change the local volume. This corresponds to a zero Lyapunov exponent. The third system, however, loses continuous spatial translation invariance after constraining the evolution to be symmetric about the origin. In this case, volume-preserving infinitesimal perturbations corresponding to pure spatial translation are no longer allowed. Thus, we lose one constraint on zero Lyapunov exponents and only one is expected to vanish in the last case.

In all cases, the numerics seem to capture accurately the presence of at least one zero Lyapunov exponent. In the third case, there is enough separation between the magnitude of exponents  $\chi_1$  and  $\chi_3$  to conclude using the error estimates only exponent  $\chi_2$  converges to zero. In the second case, two exponents appear

comparable to the error estimate of  $\sim 2 \cdot 10^{-4}$ , albeit the separation is not as evident. In the first case, only exponent  $\chi_3$  is of the same magnitude as the error estimate. The second smallest value ( $\chi_2$ ) is one order of magnitude larger, thus indicating the algorithm may struggle to converge accurately to the expected number of zero exponents.

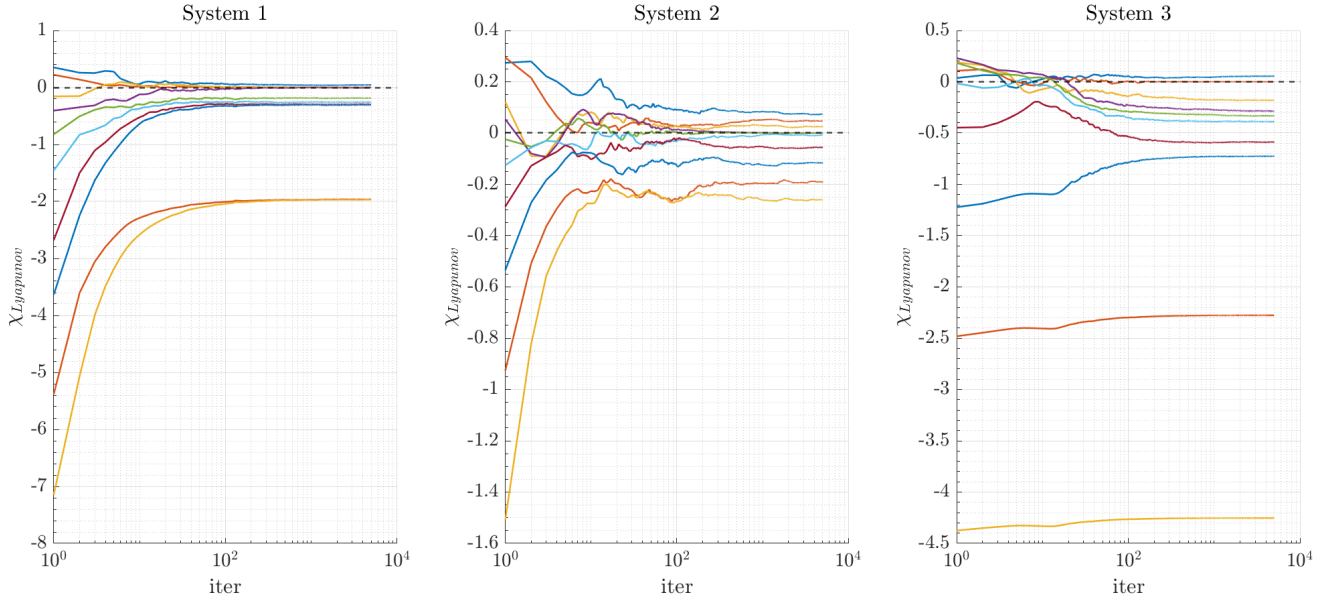


Figure 17: Ten leading Lyapunov exponents estimates. (Plot B)

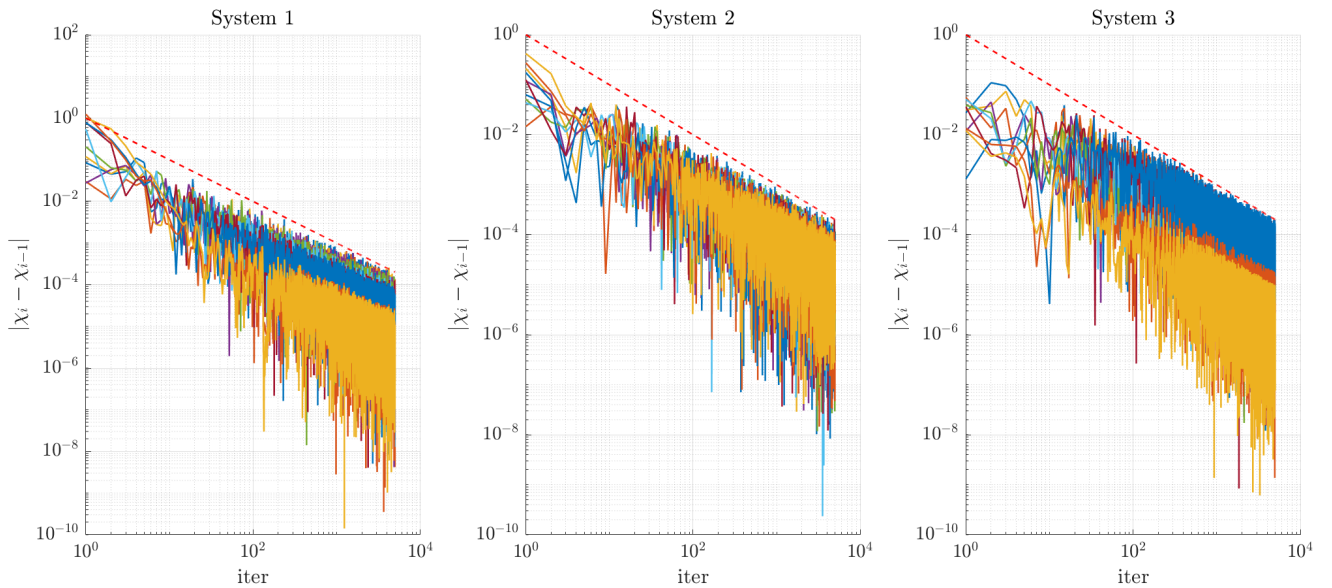


Figure 18: Convergence of leading Lyapunov exponents.

### 2.2.3 Discussion

Based on the leading positive Lyapunov exponent, the second system is the least predictable and the first one the most predictable. This is in disagreement with the qualitative interpretation in the first section. Thus, regarding unpredictability in ascending order, I would rank the systems as follows:

$$\boxed{\text{System 1} < \text{System 3} < \text{System 2}}$$

To quantify the richness or complexity of the chaotic dynamics, we resolve to the Kaplan-York dimension (31), reported at the end of the previous table. The Kaplan-York dimension is intrinsically linked to the fractal dimension of the attractor and the effective degrees of freedom in the chaotic dynamics. As can be seen, the second system presents the most complex chaotic dynamics. Contrary to the previous observation, the first system presents richer dynamics (even though more predictable) than the third one. Regarding complexity, I would rank the three systems as follows:

$$\boxed{\text{System 3} < \text{System 1} < \text{System 2}}$$

$$D_{KY} = j + \frac{\sum_{i=1}^j \chi_i}{|\chi_{i+1}|}, \quad j = \max_k : \sum_{i=1}^k \chi_i \geq 0 \quad (31)$$

Both the quantitative and qualitative analyses predict the second system to be the most unstable. The comparison between the first and third ones, however, is not straightforward by simple visual inspection of the space-time contours of the KSE. It appears it is possible to infer correctly the complexity of the attractor. However, it is more challenging to correctly capture the level of unpredictability of the chaotic system by visual inspection.

### 2.3 Periodic orbits embedded in the chaotic attractor

Unstable Periodic Orbits (UPOs) are periodic trajectories in phase space embedded in the chaotic attractor. They are of great interest in studying the statistical properties of the dynamical system as chaotic trajectories tend to shadow UPOs during their evolution. Some UPOs of the KSE attractor can be computed by a suitable convergence algorithm. First, for the convergence to be feasible, it is necessary to find a sufficiently close initial guess for the state vector and orbit period. A helpful initial estimate can be obtained by calculating the recurrence indicator (32). Low values of the recurrence indicator imply the presence of a quasi-periodicity in the time evolution of the initial state. Numerically the recurrence indicator has been computed for discretized time pairs  $(t, T)$  where  $t \leq t_{max} = 2 \cdot 10^3$  and  $T < 200$ . To avoid unnecessary computations, the time evolution of system 3 is evaluated only once up to  $t_{max}$ , and then the recurrence indicator matrix has been constructed by looking at the norm of pairwise differences of state vectors.

$$r(t, T) = \frac{\|\mathbf{v}(t) - \mathbf{v}(t - T)\|}{\|\mathbf{v}(t)\|}, \quad T < t \quad (32)$$

The computed values of the recurrence indicator for the third system are reported in Fig.19. The recurrence indicator presents identifiable structures (in blue) where the system is quasi-periodic. Even though there are regularities in their distribution, the exact shape and position of these recurring structures underline some degree of unpredictability of eventual UPOs. Ten initial guesses fed to the UPOs convergence algorithm are marked in red. These guesses have been obtained automatically by selecting the local minima of the recurrence indicator while imposing a sufficient separation between neighboring points and the bottom margin (corresponding to excessively low values of  $T$ ). The non-linear solver algorithm iteratively tries to improve the initial guess to converge towards a UPO.

The initial guesses and converged periods (for successful searches) are reported in the following table. Only six out of the ten guesses converged within the maximal number of allowable iterations (75 for the **trust-region-dogleg** minimization algorithm through the MATLAB built-in function **fso**lve).

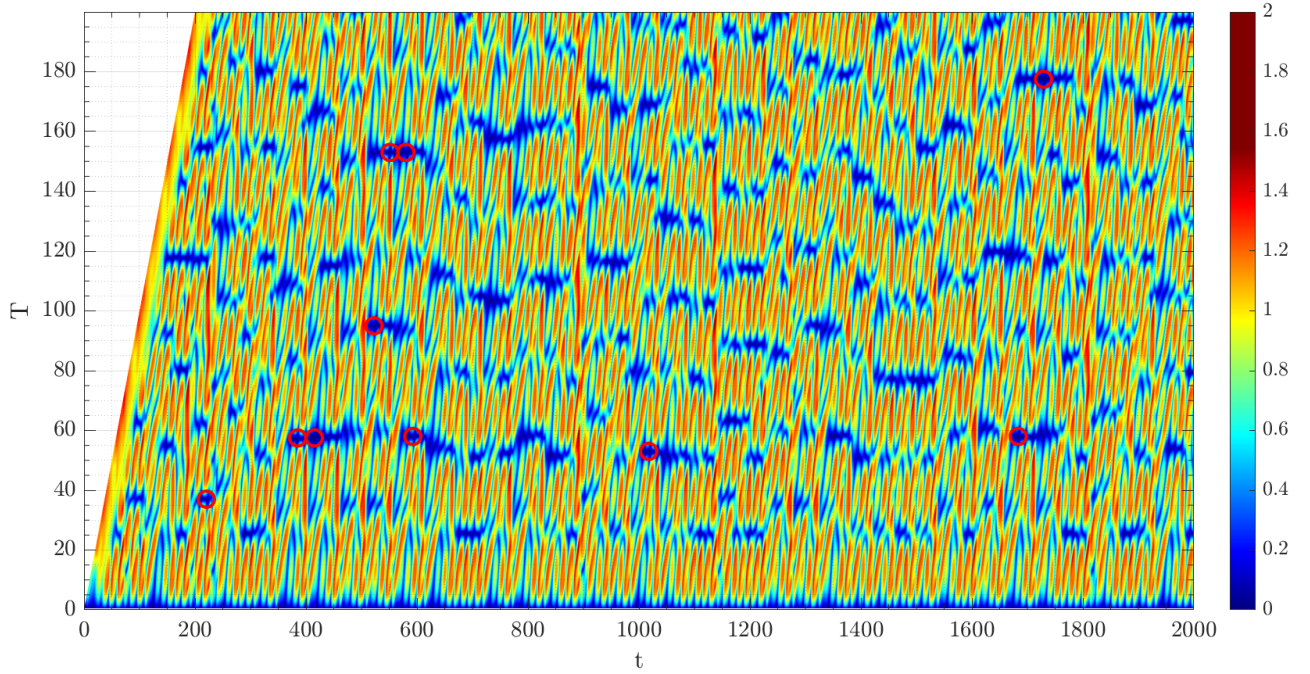


Figure 19: Recurrence indicator contours and initial guesses for orbit convergence. (Plot C)

Table 9: Table of results

guess number	guessed $t$	guessed period $T$	converged period (for successful searches)
1	551	153	-
2	1728.5	177.5	-
3	1683	58	57.933
4	592	58	57.933
5	414.5	57.5	57.933
6	1017	53	52.702
7	220	37	37.229
8	579.5	153	-
9	522	95	-
10	384.5	57.5	57.243

### 2.3.1 Discussion

The converged UPOs projected onto the first two dimensions of the state vector  $v_1, v_2$  are reported in Fig.20 and all final orbits from the optimization procedure in Fig.21. Certain periods lead more easily to a successful search. Theoretically, starting the search with an initial period that is any integer multiple of the final UPO period should lead to a successful search. In practice, any perturbation in the initial conditions will diverge exponentially in time, increasing the difficulty in finding UPOs with long periods by the numerical scheme. Three out of ten orbits converged successfully to a period  $T = 57.933$ . Moreover, two solutions (numbers 4 and 5) correspond to the same UPO as they completely overlap in the 2D projection. Even when the search is unsuccessful, there are patterns resembling the shape of converged solutions.

The converged orbits support the long-term chaotic dynamics of the KSE. The chaotic trajectory (pro-

jected onto the first two dimensions in Fig.21) clearly shows a tendency to shadow UPOs during the time system evolution. The trajectory tends to follow one particular UPO for a temporary amount of time (or cycles) until it diverges exponentially from it and shadows a different one. This process repeats leading to vibrant dynamics and fast amplification of perturbations.

In conclusion, through suitable numerical schemes, it is possible to quantify the complexity and unpredictability of the KSE chaotic attractor and to find unstable periodic orbits that are shadowed in the time evolution of the system.

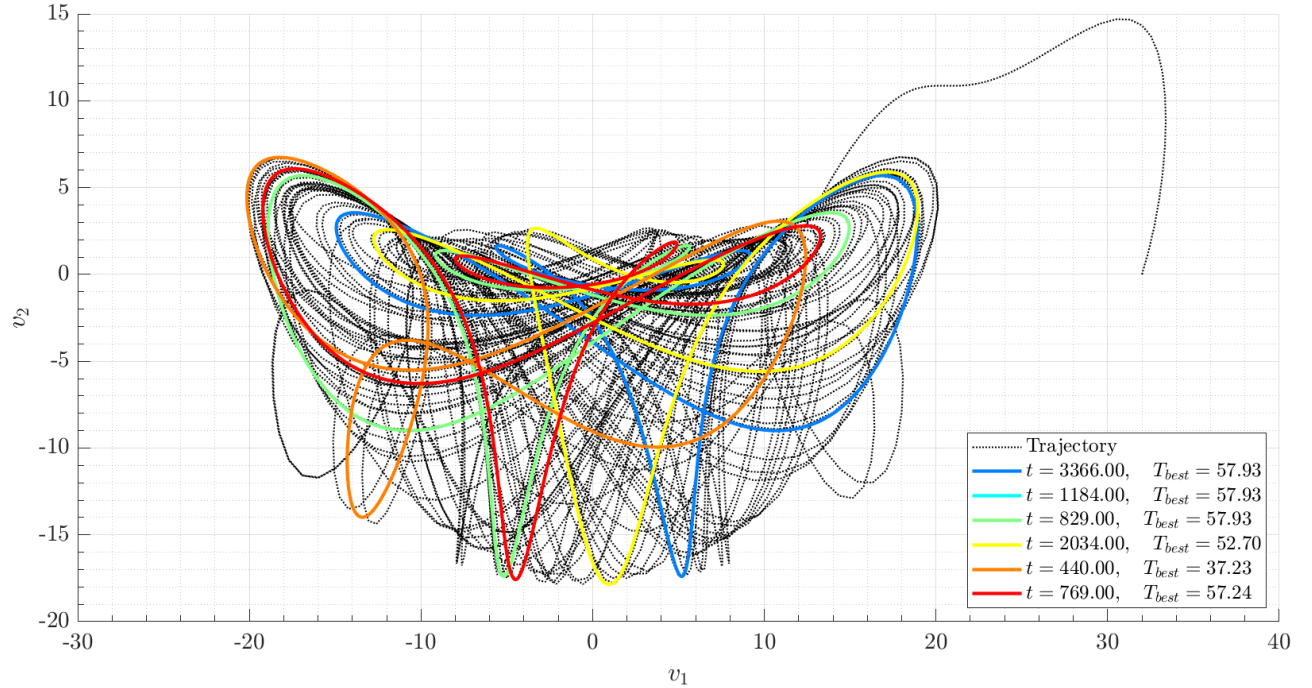


Figure 20: 2D projections of chaotic trajectory and converged orbits. (Plot D)

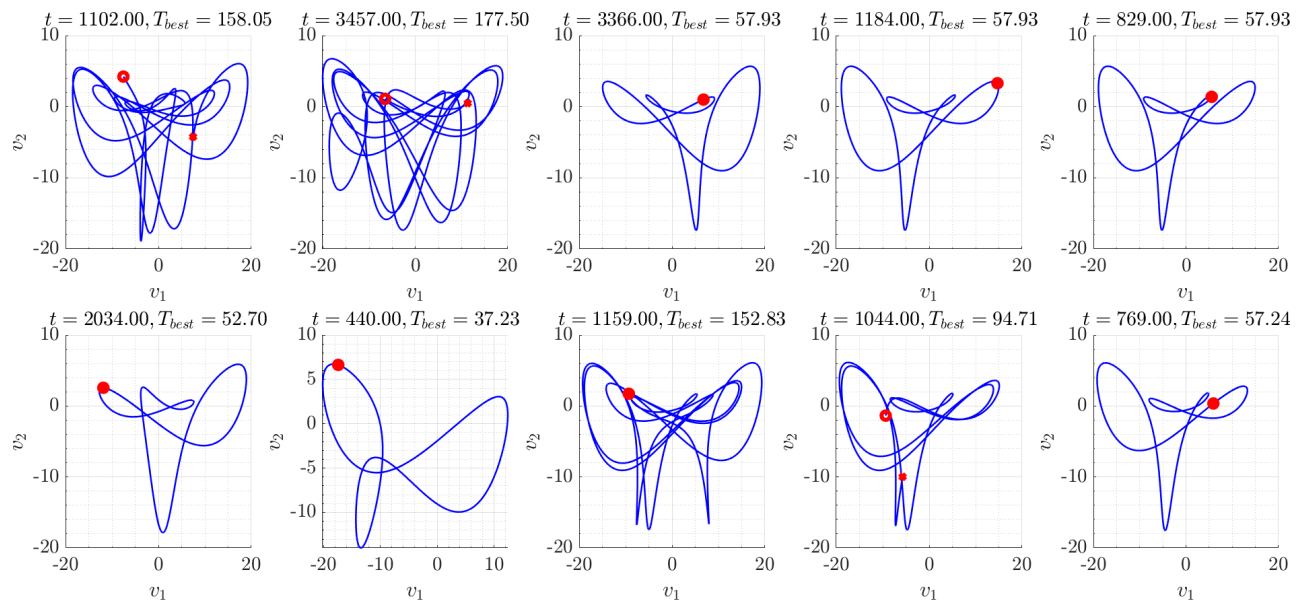


Figure 21: Final trajectories.

## Appendix

### List of Sources

- [1] Geneviève Comte-Bellot and Stanley Corrsin. Simple eulerian time correlation of full-and narrow-band velocity signals in grid-generated, ‘isotropic’ turbulence. *Journal of Fluid Mechanics*, 48(2):273–337, 1971. doi: 10.1017/S0022112071001599.
- [2] Uriel Frisch. *Turbulence: The Legacy of A. N. Kolmogorov*. Cambridge University Press, 1995.
- [3] H Haken. At least one lyapunov exponent vanishes if the trajectory of an attractor does not contain a fixed point. *Physics Letters A*, 94(2):71–72, 1983.
- [4] Aly-Khan Kassam and Lloyd N Trefethen. Fourth-order time-stepping for stiff pdes. *SIAM Journal on Scientific Computing*, 26(4):1214–1233, 2005.
- [5] Kyunghwan Yoon and Z. Warhaft. The evolution of grid-generated turbulence under conditions of stable thermal stratification. *Journal of Fluid Mechanics*, 215:601–638, 1990. doi: 10.1017/S0022112090002786.